Study of compression modes in 56Ni using an active target

Bagchi, Soumya

Chapter 2

Giant resonances and nuclear incompressibility

Giant resonances (GR) can be understood via macroscopic models but for detailed understanding, microscopic calculations have to be performed. This chapter begins with the macroscopic and microscopic descriptions of GRs. The relationship between GRs and nuclear incompressibility will be detailed. Theoretical predictions and experimental evidences of GRs in Ni isotopes closer to the subject of this manuscript will be discussed. This chapter ends with the theoretical predictions for the angular distributions of the GRs for the ^{56}Ni$(\alpha,\alpha')^{56}$Ni* reaction.

2.1 Macroscopic model

The simplest way of depicting giant resonances is through the macroscopic model where the nucleus is assumed to be a liquid drop which vibrates in different modes around its equilibrium shape. For a schematic representation of different modes of giant resonances, see Fig. 1.2. Among these giant-resonance modes, Isoscalar Giant Monopole Resonance (ISGMR) is called the "*breathing mode*" as it shows a volume oscillation around the equilibrium volume, i.e., the nucleus is either compressed or expanded with all the nuclear fluids (proton and neutron fluids) oscillating in phase. Experiments with the stable nuclei with mass number $A \geqslant 90$ show that the strength distribution for ISGMR can be described with a Gaussian. The centroid of the Gaussian (E_{ISGMR}) for nuclei with $A \geqslant 90$ can be approximated as [4]:

$$E_{ISGMR} = 80A^{-1/3}\ \text{MeV} \tag{2.1}$$

The isoscalar dipole oscillation depicted in Fig. 1.2 corresponds to a spurious center-of-mass motion. The real Isoscalar Giant Dipole Resonance (ISGDR) is a higher-order oscillation, called the "*squeezing mode*". It displays oscillations wherein the density increases on one side of the nucleus and decreases on the other side with a slight change in shape keeping the center-of-mass fixed. The centroid energy of ISGDR (E_{ISGDR}) can be approximated as [4]:

$$E_{ISGDR} = 100 - 120A^{-1/3}\ \text{MeV} \tag{2.2}$$

The strength distribution in case of ISGDR is extended over 10 MeV [4].

In both cases of ISGMR and ISGDR, there is a change of density of the nuclear matter. Therefore, these two modes are referred to as *compression modes* and are depicted in Fig. 2.1.

For comparison, Isoscalar Giant Quadrupole Resonance (ISGQR) is also depicted in Fig. 2.1. ISGQR corresponds to an axial deformation of nuclear fluid with no change in density. In lighter nuclei, the strength distribution for ISGQR is fragmented, whereas for A larger than $\sim$64, the centroid energy of ISGQR (E_{ISGQR}) can be approximated as [4]:

$$E_{ISGQR} = 64.7A^{-1/3}\ \text{MeV} \tag{2.3}$$

2.2 Microscopic model

Microscopic models have been developed to understand the nuclear structure and in particular GRs. These microscopic models are usually based on a *mean-field* concept where the nucleons are considered to move independently in a mean field generated by the two-body interaction between all nucleons in addition to a small residual interaction. Although, in principle, one can calculate the effective interaction from the bare nucleon-nucleon force, but for the sake of simplicity, the effective interaction is written in terms of phenomenological forces, e.g., Skyrme or Gogny type of interaction.

One such microscopic calculation is based on the Hartree-Fock (HF) method. In this method, one assumes that the ground state of the nucleus is approximated by a single Slater determinant of single-particle orbitals where all the states below the Fermi surface are completely

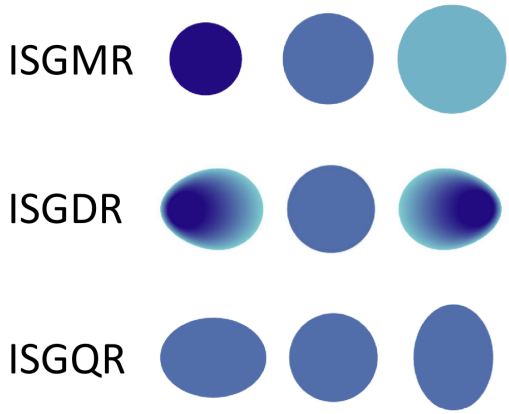

Figure 2.1: Oscillation of the nucleus about an equilibrium shape shown for ISGMR (top), ISGDR (middle), and ISGQR (bottom). The ISGMR (breathing mode) and the ISGDR (squeezing mode) display density variations and are, therefore, denoted as the compression modes. The ISGQR displays no density variations; only change in shape occurs.

filled and above the Fermi surface are completely empty. In the HF method, a *np-nh* state can be created by promoting n particles to states above the Fermi level from the states below the Fermi level. For constructing GR excitations, one has to take into account the coherent superposition of *1p-1h* transitions [4].

Nowadays, the commonly used microscopic calculation is based on Random-Phase Approximation (RPA) in which a correlated ground state of the nucleus is considered, including admixtures of *0p-0h*, *2p-2h* and higher-order configurations. Pairing correlations for open-shell nuclei can also be taken into account in the RPA formalism. In RPA, the excited state of a system can be represented by a creation operator $\hat{\Gamma}^{\dagger}_{\nu}$ acting on the correlated ground state [4]:

$$|\nu\rangle = \hat{\Gamma}^{\dagger}_{\nu}|0\rangle \tag{2.4}$$

and the ground state of the system is defined as [4]:

$$\hat{\Gamma}_{\nu}|0\rangle = 0 \tag{2.5}$$

In the lowest-order RPA, only *1p-1h* excitations are considered and the boson creation operator $\hat{\Gamma}^{\dagger}_{\nu}$ can be defined as [4]:

$$\hat{\Gamma}^{\dagger}_{\nu} = \sum_{p,h} (X^{\nu *}_{ph}\, a^{\dagger}_{p}\, a_{h} - Y^{\nu *}_{ph}\, a^{\dagger}_{h}\, a_{p}) \tag{2.6}$$

where $a^{\dagger}_{p(h)}$ is the creation operator for the particle (hole) state and $a_{p(h)}$ is the annihilation operator for the particle (hole) state. The amplitudes $X^{\nu *}_{ph}$ and $Y^{\nu *}_{ph}$ can be obtained from the particle-hole excitations under consideration.

In RPA, the transition matrix elements for an operator $\hat{O}$ ($\hat{O} = \sum_{kl} O_{kl}\, a^{\dagger}_{k}\, a_{l}$) between the ground state $|0\rangle$ and the excited state $|\nu\rangle$ is given by [4]:

$$\langle \nu | \hat{O} | 0 \rangle = \sum_{p,h} \{ X^{\nu *}_{ph}\, O^{*}_{ph} + Y^{\nu *}_{ph}\, O_{hp} \} \tag{2.7}$$

The moment of an electric multipole transition can be expressed in terms of spherical Bessel function. Depending on the multipolarities of the isoscalar giant resonances, either the first-order term or the second-order term of the expansion of the Bessel function should be considered. In case of ISGMR ($L = 0$), the first-order term is a constant. In case of ISGDR ($L = 1$), the first-order term corresponds to a translational motion of the whole nucleus and it is not an intrinsic nuclear excitation. Therefore, the transition operators for the isoscalar electric giant resonances can be written as:

$$\begin{aligned} \hat{O}_{L} &= \sum_{i=1}^{A} r_{i}^{L}\, Y_{LM}(\Omega_{i}), \qquad L \geqslant 2 \\ \hat{O}_{L} &= \frac{1}{2} \sum_{i=1}^{A} r_{i}^{L+2}\, Y_{LM}(\Omega_{i}), \qquad L < 2 \end{aligned} \tag{2.8}$$

with $Y_{LM}(\Omega_{i})$ being the spherical harmonics. The qualitative features of giant resonances can be understood from a schematic shell-model picture as shown in Fig. 2.2. The parity of the single-particle wave functions in the subsequent shells N, $N+1$, $N+2$, ... are alternating. Due to parity conservation, odd multipolarity transitions require ΔN = 1, 3, ... and even multipolarity transitions require ΔN = 0, 2, ... However, $0\hbar\omega$ transition is not possible for ISGMR because of angular-momentum conservation. In this model, the energy difference between two major shells is [4]:

$$\Delta E = \Delta N \times 1\hbar\omega = \Delta N \times 41 A^{-\frac{1}{3}}\ \text{MeV} \tag{2.9}$$

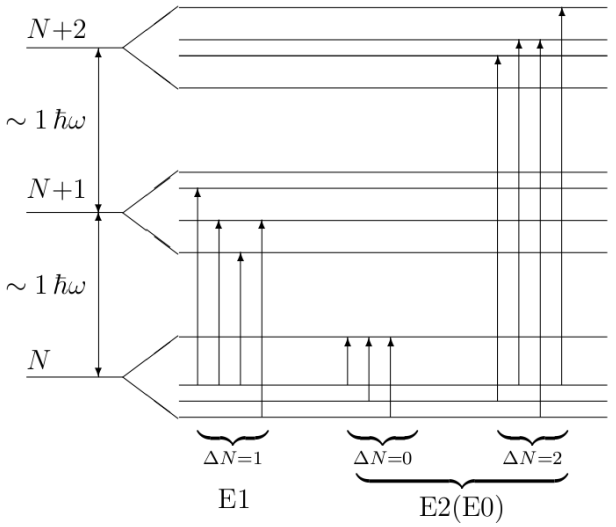

Figure 2.2: Schematic picture of $E1$ and $E2$ ($E0$) single-particle transitions between shell-model states [4].

Since the residual particle-hole interaction is attractive for isoscalar excitations and repulsive for isovector excitations, the isoscalar resonances will be located below and the isovector resonances will be located above the corresponding unperturbed energies $\Delta N \times 41 A^{-\frac{1}{3}}$ MeV. In fact, it has been found experimentally that ISGQR and IVGDR are located nearly at same excitation energy. Therefore, it is necessary to use specific probes to disentangle the overlapping resonances.

2.3 Sum rules

The strength function of a transition can be obtained from the transition matrix elements from Eqn. 2.7:

$$S_F(E) = \sum_{\nu} |\left\langle \nu|\hat{O}|0\right\rangle|^2 \delta(E - E_\nu) \tag{2.10}$$

where $\hat{O}$ is the transition operator between the ground state $|0\rangle$ and the excited state $|\nu\rangle$ at energy E_ν. One can define the n^{th} moment of the strength distribution by [31,32]:

$$m_n = \sum_\nu (E_\nu - E_0)^n \mid \langle \nu | \hat{O} | 0 \rangle \mid^2 \tag{2.11}$$

The sum turns into an integral for continuum states. By taking appropriate ratios of these moments, one can obtain various estimations for the energy of the monopole vibration. The first-order moment m_1 can be written as:

$$m_1 = \sum_\nu (E_\nu - E_0) \mid \langle \nu | \hat{O} | 0 \rangle \mid^2 \tag{2.12}$$

This first-order moment is used to characterize the giant resonances and is defined as the Energy-Weighted Sum Rule (EWSR). It can be evaluated model independently. For isoscalar resonances, it depends only on the ground-state properties of the nucleus. A giant resonance state exhausts almost all of the transition strength. Usually for heavier nuclei with $A \geq 90$, the giant resonance state exhausts about 100% of the EWSR whereas for lighter nuclei it exhausts $50 - 100\%$ of the EWSR.

2.4 Damping of giant resonances

2.4.1 Width of the resonances

The GRs are characterized by their broad widths. The total width of the giant resonance can be defined as [4]:

$$\Gamma_{total} = \Gamma_{inh} + \Gamma^{\downarrow} + \Gamma^{\uparrow} \tag{2.13}$$

where Γ_{inh} is the *inherent* width, $\Gamma^{\downarrow}$ is the *spreading* width and $\Gamma^{\uparrow}$ is the *escape* width. Among these, the *spreading* width gives the largest contribution to the total width.

The *inherent* width (commonly called Landau damping) is due to the spreading in excitation energy of the initial collective *1p-1h* transitions. Such a spreading can be caused by many non-collective *1p-1h* transitions whose energies are close to the energy of the collective state.

The *spreading* width arises from the coupling of the *1p-1h* configurations with the *2p-2h*, *3p-3h* and higher-order configurations. For the theoretical understanding of the *spreading* width, RPA calculations are required where the admixtures of *2p-2h* and higher-order configurations are considered.

The *escape* width can be understood from the decay of the giant-resonant state. In general,

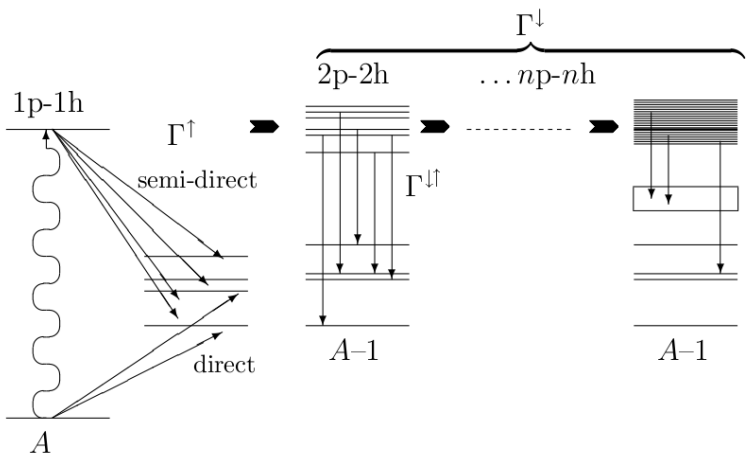

Figure 2.3: Processes by which a giant-resonance state acquire a width, are shown schematically. $\Gamma^{\uparrow}$ is the escape width and $\Gamma^{\downarrow}$ is the spreading width [4].

the collective *1p-1h* state is well above the particle-emission threshold. Therefore, the state acquire a width through particle emission. In principle, the *2p-2h*, ... states can also decay by particle emission which is denoted as $\Gamma^{\downarrow\uparrow}$. In Fig. 2.3, the processes which lead to the GR state acquiring a width are illustrated schematically.

2.4.2 Decay of giant resonances

Since the GR states are well above the particle emission threshold, their properties can be determined by studying their particle decay. The spin and parity of the GR state can also be determined by looking into the angular correlations between the ejectile and the decay particle [33, 34]. Furthermore, since GRs are sitting on top of a continuum, the background can be eliminated by performing coincidence measurements between the ejectile from the GR excitation process and the decay particles (neutron, proton, α, γ) [35, 36].

2.5 Nuclear incompressibility

The incompressibility of nuclear matter (K_∞) is a basic quantity like saturation density (ρ_0) or Fermi momentum (k_F). It can be defined as the curvature of the binding energy per

particle at the saturation density (ρ_0) and can be written as [37]:

$$K_\infty = 9\rho_0^2 \frac{d^2(E/A)}{d\rho^2}\bigg|_{\rho_0} \tag{2.14}$$

Nuclear incompressibility is an important ingredient in the equation of state of nuclear matter. Its value enters into the analysis of astrophysical phenomena such as masses of neutron stars and explosion of supernovae. However, unlike the equilibrium density, the value of nuclear incompressibility cannot be measured directly. It turns out that the best way to determine K_∞ is from the strength distributions of the ISGMR and the ISGDR which can be experimentally accessed. The centroid energies of the ISGMR and ISGDR, the so-called compression modes, are given in the constrained and scaling models as [38]:

$$E_{ISGMR} = \hbar\sqrt{\frac{K_A}{m < r^2 >}} \tag{2.15}$$

$$E_{ISGDR} = \hbar\sqrt{\frac{7}{3}\frac{K_A + \frac{27}{25}\epsilon_F}{m < r^2 >}} \tag{2.16}$$

where E_{ISGMR} and E_{ISGDR} are the centroid energies of ISGMR and ISGDR, respectively, m is the nucleon-mass, $\langle r^2 \rangle$ is the mean-square nuclear radius and ϵ_F is the Fermi energy. One can see that if the excitation energies of the compression modes increase the nucleus becomes harder. In the above equations, K_A is the nuclear incompressibility for a finite nucleus. Following the liquid-drop model concepts, K_A can be expanded as follows [39]:

$$K_A = K_\infty + K_{surf}A^{-1/3} + K_\tau\left(\frac{N-Z}{A}\right)^2 + K_{Coul}Z^2A^{-4/3} \tag{2.17}$$

where K_∞ is the volume term and is the nuclear incompressibility for infinite nuclear matter. K_{surf}, K_τ, and K_{Coul} are surface, neutron-proton asymmetry and Coulomb terms, respectively. However, in this model, the values of K_∞ from the fit of the data using Eqn. 2.17 do not converge to a unique solution but a good fit can be obtained giving values of K_∞ ranging from 100 MeV to 400 MeV [32, 40].

The microscopic calculations of nuclear incompressibility depend on the possibility of constructing sets of effective interactions, e.g., Skyrme or Gogny interactions. These effective interactions can reproduce well the nuclear properties such as binding energy, Fermi mo-

mentum and charge radius. By calculating the energy of the breathing mode with such effective interactions, one can correlate the value of K_A for a nucleus with the corresponding value of K_∞ in nuclear matter.

The value of K_∞ obtained from the ISGMR & ISGDR data is 240$\pm$10 MeV [41–44]. The effective interactions mentioned above can reproduce well the centroid energies of the ISGMR for ^{90}Zr, ^{144}Sm, and ^{208}Pb [45]. However, the same effective interactions overestimate the centroid energies for ISGMR strength distributions for Sn [46, 47] and Cd [48] isotopes, although they can reproduce well the ground-state properties for Sn and Cd isotopes. In spite of significant theoretical efforts to reproduce simultaneously the ISGMR centroid energies in ^{90}Zr, ^{208}Pb, and in Sn/Cd isotopes, no single approach has emerged. Therefore, in order to help solving the mystery *why Sn or Cd isotopes are fluffy* [46–48], it is necessary to study compression modes for another series of isotopes. Since Ni isotopes have astrophysical implications, efforts have been put to study in details the compression modes for several stable and unstable isotopes of Ni from the proton-rich to neutron-rich regions of the nuclear chart.

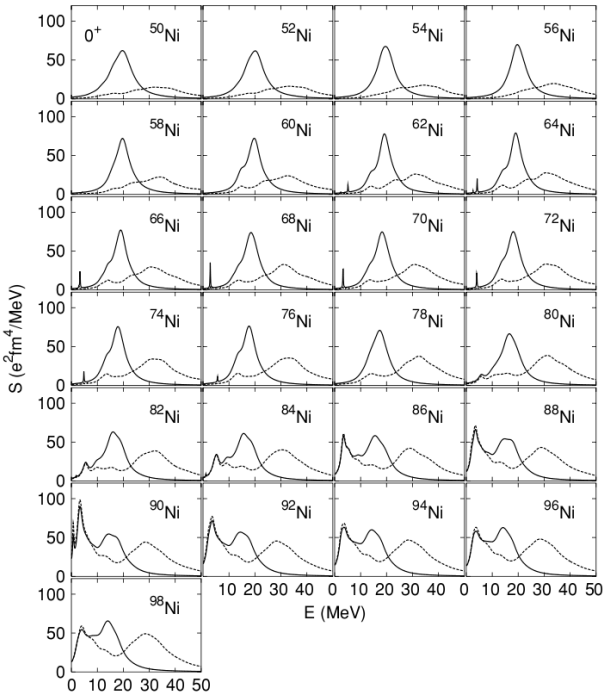

Figure 2.4: $E0$ strength functions for even-A Ni isotopes. The solid line refers to isoscalar modes and the dashed line refers to isovector modes [49].

2.6 Giant resonances in Ni isotopes

2.6.1 Theoretical predictions

Giant resonances have been extensively studied for stable isotopes. But for exotic nuclei there is little information available. To understand different terms in Eqn. 2.17 and especially the term K_τ, the asymmetry term, one has to study the giant resonances over an isotopic chain of an element. In Figs. 2.4, 2.5, and 2.6, the theoretical predictions for GMR, GDR, and GQR for both isoscalar and isovector modes for even-A Ni isotopes from the proton-drip line to the neutron-drip line are given. The calculations were done using Quasi-particle RPA (QRPA) with three types of Skyrme interactions (SkM*, Skp, and Sly4). The results for different Skyrme interactions are essentially very similar [49].

In Fig. 2.4, the 0^+ strength functions for isoscalar and isovector modes are given for Skyrme interaction of type SkM*. The isoscalar giant resonance peaks at around 20 MeV and gradually moves to around 15 MeV as N, the number of neutrons, increases. The isovector giant resonance is broad in the light isotopes and develops a low-energy component as N gets larger.

In Fig. 2.5, the 1^- strength functions for isoscalar and isovector modes are given for Skyrme interaction of type SkM*. The isoscalar giant resonance peak appears around 30 MeV and develops a low-energy component as N increases. The isovector giant resonance peak appears around 16 MeV.

In Fig. 2.6, the 2^+ strength functions for isoscalar and isovector modes are given for Skyrme interaction of type SkM*. The isoscalar giant resonance peak appears around 16 MeV and shifts to lower energies as N increases. The centroid of the isovector resonance peak appears to be around 30 MeV and decreases as N increases.

2.6.2 Experimental evidences

Previous studies from Texas A&M University [50] of the giant resonance regions in stable ^{58}Ni and ^{60}Ni isotopes were performed with inelastic scattering of α-particles at an incident beam energy of 240 MeV. In Fig. 2.7, the strength distributions for $E0$, $E1$, $E2$, and $E3$ isoscalar transitions are shown for ^{58}Ni. In Fig. 2.8, the strength distributions for $E0$, $E1$, $E2$, and $E3$ isoscalar transitions are shown for ^{60}Ni.

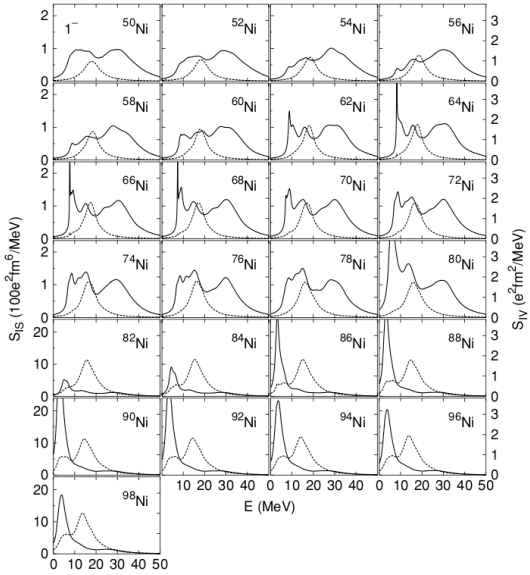

Figure 2.5: Same as Fig. 2.4 but for $E1$ [49].

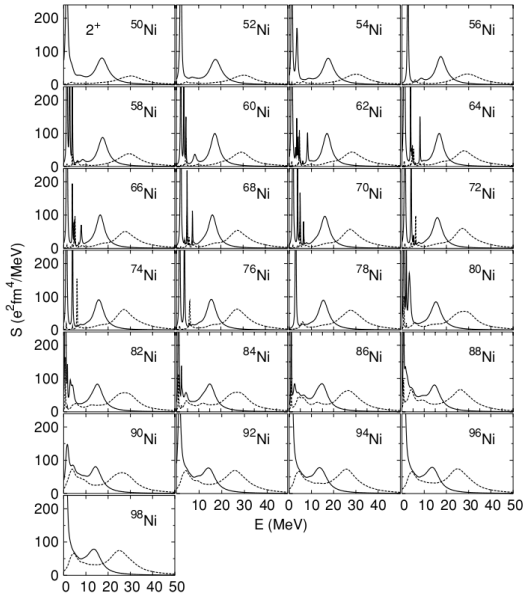

Figure 2.6: Same as Fig. 2.4 but for $E2$ [49].

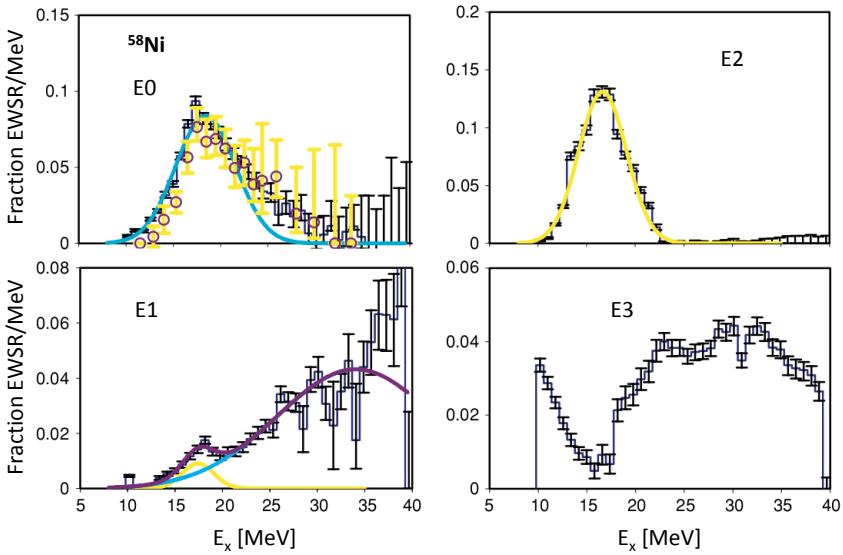

Figure 2.7: $E0$, $E1$, and $E2$ strength distributions are shown for ^{58}Ni. $E3$ distribution includes all $L \geq 3$ strengths [50]. The curves represent the Gaussian fits to the data. The open circles in the $E0$ strength distribution are from Ref [51].

ISGMR, ISGDR, and ISGQR in ^{58}Ni have also been studied by Nayak et al. [52] at RCNP with inelastic α-particle scattering at 386 MeV incident energy. In both cases, the centroid energies of ISGMR and ISGQR have been found to be around 19 MeV and 16 MeV, respectively. In case of ISGDR, there is evidence for a "bi-modal" strength distribution for ^{58}Ni and ^{60}Ni with the high-energy peak appearing around 30 MeV.

ISGMR and ISGQR for the exotic neutron-deficient nucleus ^{56}Ni have been studied by Monrozeau et al. [53], by inelastic deuteron scattering in inverse kinematics with a ^{56}Ni beam at an incident energy of 50 MeV/u. The experiment was performed at the GANIL facility using the active target MAYA. In the left panel of Fig. 2.9, the efficiency-corrected excitation energy is shown with the Gaussian fits for ISGQR and ISGMR. In the right panel of Fig. 2.9, the cross sections obtained from the Gaussian fits are shown. The excitation energy of ISGMR has been found to be 19.3$\pm$0.5 MeV with almost 136% exhaustion of the EWSR. The excitation energy of ISGQR has been found to be 16.2$\pm$0.5 MeV with almost 76% exhaustion of the EWSR.

Giant resonances have also been studied for neutron-rich ^{68}Ni by Vandebrouck et al. [54],

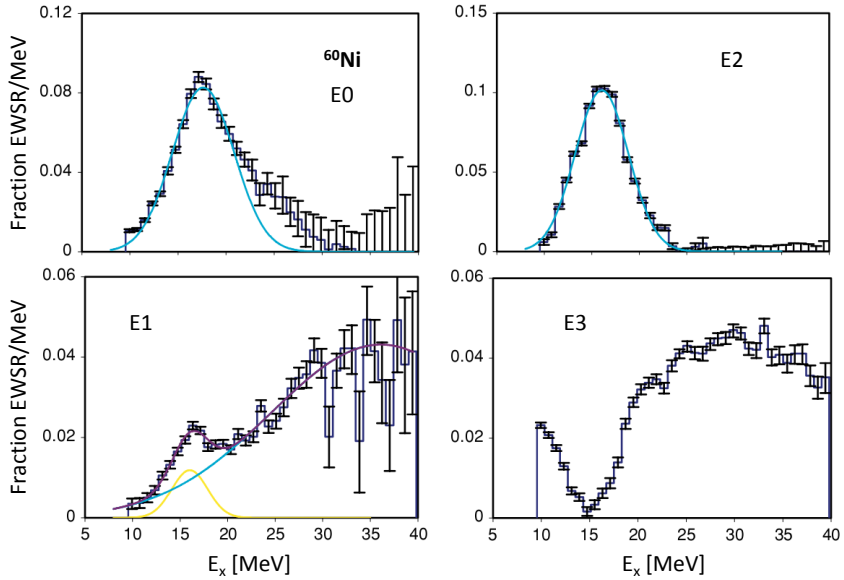

Figure 2.8: Same as Fig. 2.7 but for ^{60}Ni [50]. The curves represent the Gaussian fits to the data.

by inelastic α-particle and deuteron scattering in inverse kinematics with a ^{68}Ni beam at an incident energy of 50 MeV/u. This experiment was also performed at the GANIL facility using active target MAYA. In Fig. 2.10, the total excitation-energy spectrum of ^{68}Ni and excitation-energy spectrum of ^{68}Ni at 5.5° CM angle are shown with the Lorentzian fits for ISGMR, ISGQR, and also for the soft-monopole mode which reflects the collectivity due to extra neutrons relative to protons. In the right panel of Fig. 2.10, the angular distributions obtained from the Lorentzian fits are also shown for the soft-monopole mode and the ISGMR. The excitation energy of ISGMR for ^{68}Ni from the Lorentzian method has been found to be 21.1$\pm$1.9 MeV. For comparison of the results obtained from different experiments see Chapter 6.

2.7 Theoretical predictions for angular distributions

Theoretical predictions of the angular distributions for the ISGQR, ISGMR, and ISGDR are necessary to identify the nature of the GRs excited in the inelastic α-scattering experiments. Here, they have been made in the framework of the Distorted-Wave Born Approximation

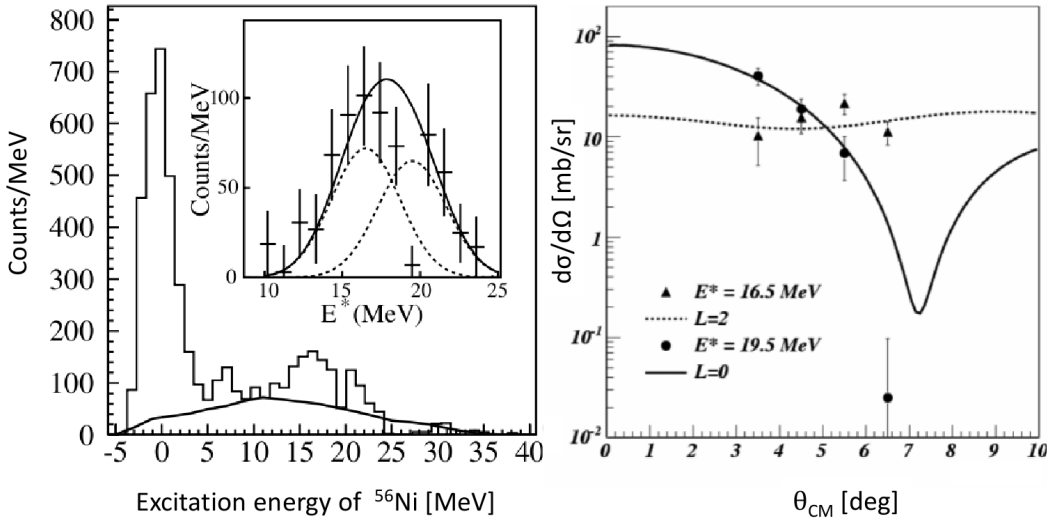

Figure 2.9: Left panel: ^{56}Ni excitation-energy spectrum corrected for geometrical efficiencies. The background due to deuteron break-up is shown by the solid line. The inset shows the background subtracted inelastic data fitted with Gaussian distributions located at 16.5 MeV and 19.5 MeV for the ISGQR and ISGMR, respectively. Right panel: cross sections for ISGQR (triangles) and ISGMR (filled circles) obtained from the Gaussian fits [53].

(DWBA). This formalism will be only briefly detailed, since the aim is to present the conditions under which the calculations were performed. Details of the method can be found in Refs. [4, 55].

2.7.1 General formalism

To describe the scattering process one needs to solve the time-dependent Schrödinger equation using Fermi's Golden rule. In this case, it is assumed that the potential vanishes faster than $1/r$ for large r, where r is the spatial coordinate. Since the incident particles are monoenergetic, the incident wave can be considered as a plane wave. The scattered particle can be considered as an outgoing spherical wave. The scattering wave function must fulfill the boundary conditions, i.e., being finite at the origin and showing asymptotic behavior at large r. The scattering wave function is given by:

$$\psi(\mathbf{k},\mathbf{r}) \xrightarrow{r\to\infty} e^{i\mathbf{k}.\mathbf{r}} + f(\theta,\phi)\frac{e^{ikr}}{r} \tag{2.18}$$

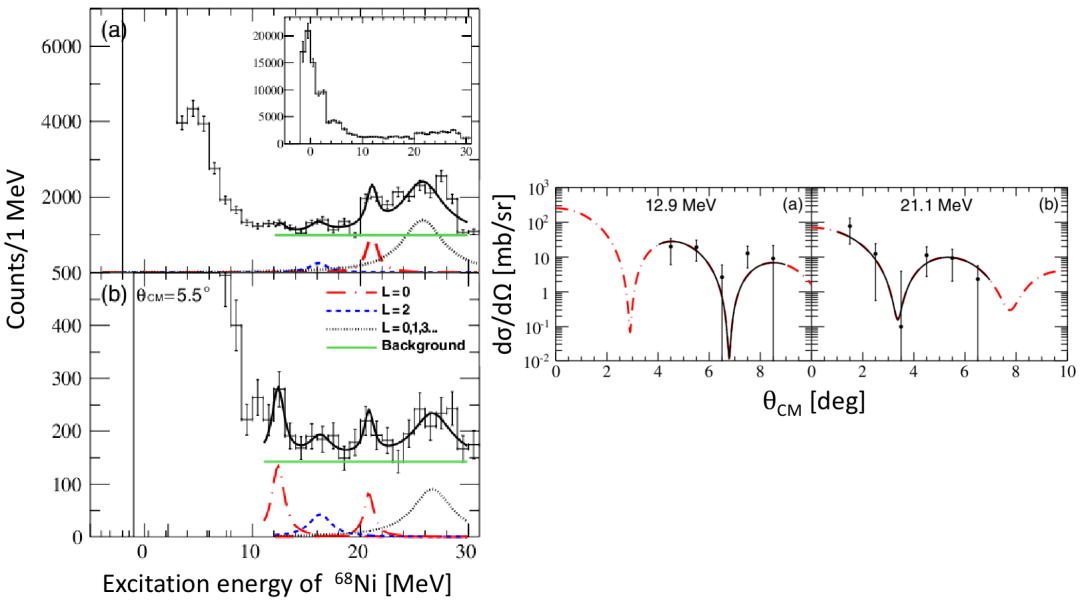

Figure 2.10: Left panel: (a) ^{68}Ni excitation-energy spectrum for all angles deduced from the alpha recoil kinematics and corrected for geometrical and reconstruction efficiencies. (b) Same for $\theta_{CM} = 5.5°$. For both spectra, the subtracted background is indicated by the horizontal green solid line. The data were fitted with Lorentzians at 12.9 MeV (red dot-dashed line), 15.9 MeV (blue short-dashed line), and 21.1 MeV (red dot-dashed line) for the low-energy mode, the ISGQR, and the ISGMR, respectively. Right panel: Angular distributions for the modes located at 12.9 MeV (a) and 21.1 MeV (b). The black solid line corresponds to the fit based on DWBA calculation using microscopic RPA predictions with isoscalar $L = 0$ multipolarity. These predictions are represented by red dot-dashed lines [54].

where $\mathbf{r}$ is the spatial vector, $\mathbf{k}$ is the wave vector and $e^{i\mathbf{k}.\mathbf{r}}$ is the incoming plane wave. The second term on the right hand side of Eqn. 2.18 represents the outgoing spherical wave, where $f(\theta, \phi)$ is the scattering amplitude. The differential cross section is simply the square of the scattering amplitude:

$$\frac{d\sigma}{d\Omega} = |f(\theta, \phi)|^2 \tag{2.19}$$

2.7.2 The optical potential

In the optical model, the potential is referred to as *optical potential*. In the case of α-particles (spin 0), it contains real and imaginary volume potentials and can be defined as:

E_α	240 MeV
V_{o_R}	76.6 MeV
V_{o_I}	24.2 MeV
R_R	4.75 fm
R_I	5.49 fm
r_C	1.3 fm
a_R	0.8 fm
a_I	0.8 fm

Table 2.1: Optical-model parameters obtained by Clark et al. [57].

$$U(r) = V(r) + iW(r) \tag{2.20}$$

where $V(r)$ is the real potential and it corresponds to the coupling to the elastic channel where there is no change in particle flux in the output channel. $W(r)$ is the imaginary part and it arises because of the coupling to all non-elastic channels (e.g., inelastic scattering, transfer reactions etc.). A potential well of the Woods-Saxon type [56] is usually taken for both the real and imaginary terms and is given for the real potential by:

$$V(r) = -V_o f(r) = -\frac{V_o}{1 + exp(\frac{r-R}{a})} \tag{2.21}$$

where V_o is the depth of the potential, R its radius and a its diffuseness. The parameters are adjusted in a way that the cross-sections calculations for the elastic scattering and the first excited state of ^{58}Ni agree with the experimental data. Clark et al. [57] measured the α-particle elastic scattering and inelastic scattering differential cross sections for ^{58}Ni. By fitting the data, they obtained the optical-potential parameters which are listed in Table 2.1. The same parameter values have been used in this thesis to obtain the angular distributions of the GRs in ^{56}Ni, since 240 MeV total energy for the α-particle corresponds to 60 MeV/u which is not that different from the 50 MeV/u beam energy used for the experiment presented in this thesis. Furthermore, the number of nucleons in ^{56}Ni is nearly equal to ^{58}Ni.

2.7.3 DWBA approximation

The DWBA is an approximation that takes into account the first-order coupling between the initial state and final state as well as the effect of the distortion of the incident wave and the

scattered wave due to the optical potential acting between the projectile and the target. The transition matrix element between the initial state i (^{56}Ni and α-particle) and the final state f (scattered ^{56}Ni and recoil α-particle) can be written as [58]:

$$T_{fi} \propto \int \chi_f^{(-)}(\vec{r}) \, \langle f|\delta U(\vec{r})|i\rangle \, \chi_i^{(+)}(\vec{r}) d\vec{r} \tag{2.22}$$

where $\vec{r}$ is the relative position between the target and the projectile. $\chi_f^{(-)}$ and $\chi_i^{(+)}$ are the distorted waves for the output channel (after scattering) and input channel (before scattering), respectively. $\delta U(\vec{r})$ is the perturbed potential caused by the residual interaction and is responsible for inelastic excitations of the nucleus after the scattering. The matrix element $\langle f|\delta U(\vec{r})|i\rangle$ contains all the information about the structure of the initial and final states and the interaction responsible for the transition. From the transition matrix element, it is easy to calculate the differential cross section:

$$\frac{d\sigma}{d\Omega} = \left(\frac{\mu}{2\pi\hbar^2}\right)^2 \frac{k_i}{k_f} \, |T_{fi}|^2 \tag{2.23}$$

where μ is the reduced mass of the target and the projectile, k_i and k_f are the incoming and outgoing wave numbers.

2.7.4 DWBA for ^{56}Ni(α, α')^{56}Ni* reaction

The centroid energy of ISGQR in ^{56}Ni is located around 16.5 MeV [53], the centroid energy of ISGMR in ^{56}Ni is located around 19.5 MeV [53], and the centroid energy of ISGDR (with $\geq$ 50% EWSR exhausted) in ^{58}Ni is located around 30.5 MeV [52]. DWBA calculations are performed for ^{56}Ni(α, α')^{56}Ni* reaction considering the excitation energy of ^{56}Ni to be at 16.5 MeV, 19.5 MeV, and 30.5 MeV for ISGQR, ISGMR and ISGDR, respectively. In these calculations, it has been assumed that there is 100% exhaustion of the EWSR. The results are shown in Fig. 2.11.

The DWBA calculations were performed using the CHUCK3 code [59]. The parameters of the optical potential used to calculate the cross sections are listed in Table 2.1. As can be seen from Fig. 2.11, we have to measure the cross sections of the giant resonances at forward angles because as the CM angle increases the cross section diminishes by orders of magnitude. Furthermore, the angular distributions at forward angles are characteristic of the multipolarity. For example, to measure the ISGDR, it is good to measure it between

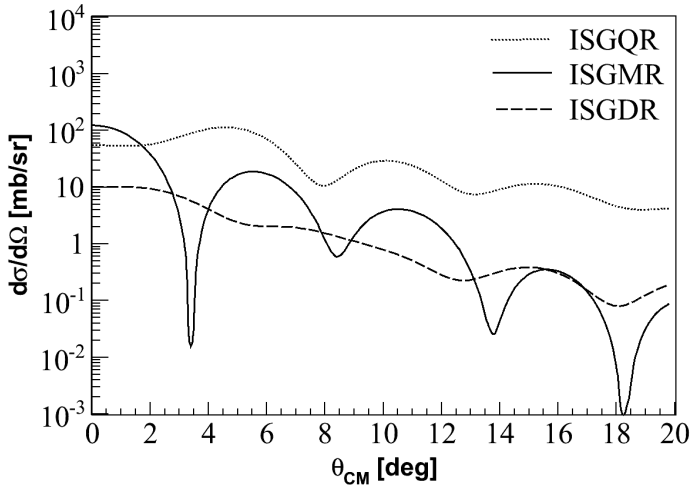

Figure 2.11: DWBA calculations for ISGMR, ISGDR, and ISGQR as described in the text.

3° and 4° CM angle, where the first minimum of the ISGMR cross section appears. The forward-angle measurement leads to detection of recoil α-particles having energies less than around 5 MeV. Since the active target MAYA has low detection threshold, it is best suited to study the compression modes, i.e., ISGMR and ISGDR in ^{56}Ni.